JOURNAL OF SPACECRAFT AND ROCKETS
Vol. 38, No. 2, March–April 2001

Aerodynamic Performance of a Rotate-to-View Nose Missile

B. Srivastava* and J. Furtek†
Raytheon Electronic Systems, Tewksbury, Massachusetts 01876

Computational fluid dynamics predictions are compared with the wind-tunnel tests for a missile consisting of a rotate-to-view nose with a flat optical window, puffed-up side cheeks, a roll-control nose strake, a tail-mounting assembly with four control panels, and other missile surface appendages. Validation results are presented for subsonic, transonic, and supersonic Mach numbers of 0.8, 0.97, 1.05, 2.0, 3.5, and 4.5 at angles of attack ranging from 10 to 65 deg. Good overall comparisons of the predicted forces and center-of-pressure locations are shown for this very complex geometry. Application studies are then presented to estimate the captive flight interference effects using a multibody computational simulation model consisting of a wing with two missiles mounted on pylons. Results are also presented to show the aero-optical wavefront distortion of the flat infrared window for a seeker orientation using a coupled computational fluid dynamics and optical analysis.

Nomenclature

CM	=	$F_N \cdot (X_{mc} - X_{cp})/(q \cdot S \cdot X_{ref})$
CN	=	normal force coefficient, $CN = (N/q \cdot S)$
D	=	forebody missile diameter, in.
M	=	freestream Mach number
N	=	normal force, lbf
P	=	pressure, lbf/in.^{2}
q	=	dynamic pressure, $q = \frac{1}{2}\rho v^2$
S	=	missile cross-sectional area, in.^{2}
v	=	velocity, ft/s
X_{cp}	=	center-of-pressure location, in.
X_{mc}	=	moment reference distance
X_{ref}	=	reference length, missile diameter
α	=	angle of attack, deg
γ	=	ratio of specific heats
ρ	=	density
ϕ	=	azimuth angle, deg

Introduction

ACCURATE prediction of aerodynamic force and moments for an arbitrary shaped missile is of critical importance to the airframe designer. The target effectiveness of a missile is dependent on its ability to achieve the desirable aerodynamic qualities in free flight as well as in an interference flowfield. Advanced concepts are currently being developed either for performance improvement of the existing system for new missions or for new concept development for future missions. These new concepts do not have legacy database or appropriate design tools that can aid a designer in the preliminary design phase. For this reason computational fluid dynamics (CFD) methodology is playing an increasing role during the design and development phase of such missiles. This methodology has the potential to provide a vast amount of valuable information for design provided proper care is taken to establish the validity of such procedures through extensive comparisons with relevant wind-tunnel data.

This paper addresses the aerodynamic issues associated with a RTV (rotate-to-view) nose missile as shown in Fig. 1. It is observed from the missile geometry details that it is an unconventional missile with a flat window on the nose and a nose strake that is used to control the roll moment of the nose. The step down in the diameter represents the end of the nose part that rotates around the missile axis for wide-view target recognition. Additional complexity of the geometry consists of the external wire cover for the entire length of the missile and fins with fin-mounting assembly as shown in Fig. 1. All of these components, along with the nose shape, creates a concept that has no legacy design basis. For this case, thus, a unique blend of wind-tunnel tests and CFD methodology must be adopted to evolve a cost-effective design basis. This paper addresses several aspects of the missile design, such as validation of the force and moment coefficients for the basic missile geometry with wind-tunnel tests at subsonic, transonic, and supersonic flows, CFD evaluation of the nose rolling moment and its comparison with the wind-tunnel test, and CFD validation of the entire missile including all of the geometrical details. After having established some confidence using data comparisons, further application studies are conducted for captive flight interference effects on the nose roll moment and optical quality of the nose window. For the latter two case studies, wind-tunnel data were not available.

Received 11 January 1999; presented as Paper 99-1068 at the AIAA 37th Aerospace Sciences Meeting, Reno, NV, 11–14 January 1999; revision received 10 January 2000; accepted for publication 24 January 2000.

*Senior Development Engineer; currently Lead Engineer, General Electric Aircraft Engine, Lynn, MA 01910. Senior Member AIAA.
†Member of Technical Staff, System Design Laboratory.

Background

Computation of complex geometry has numerous challenges. At high angles of attack this geometrical challenge is coupled with flow physics that are extremely complex in nature. It is somewhat difficult to enumerate the numerous excellent contributions of many researchers in this area. An attempt will be made here to cite some recent efforts that contain comparisons with the experimental data.

The current author's research for missiles has primarily focused on cone cylinder for missile body and simple fin shapes with divert jets for supersonic missile control.[1–6] For such cases extensive computational studies with and without divert jets show excellent comparisons of the predicted results for supersonic flows. Current efforts are now being directed toward subsonic and transonic flows with complex geometrical configuration. This paper is a step in this direction. Recent Navier–Stokes computations[7–10] around complex bodies show encouraging agreement with available experimental data. Additional computations were reported,[11,12] where the researchers studied a full missile configuration at low subsonic speeds and high angles of attack. These computations were found to be in good agreement with the available experimental data. These computations, however, were for a blunt smooth nose unlike the current nose shape shown in Fig. 1. The optical window on the missile nose causes geometrical complexity and attendant flow complexity, which are addressed in this paper.

Computational Methodology

The missile geometry as seen in Fig. 1 consists of a modified cylinder of diameter 5.75 in. and a step-down cylinder of diameter 5 in. The forebody shape is a complex combination of cylinder-ellipsoid and flat (window) surfaces which can only be described through a CAD package.

PARCH,[13] which is a full Navier–Stokes (FNS) code with plume/missile airframe steady-flow predictive capability, is being used

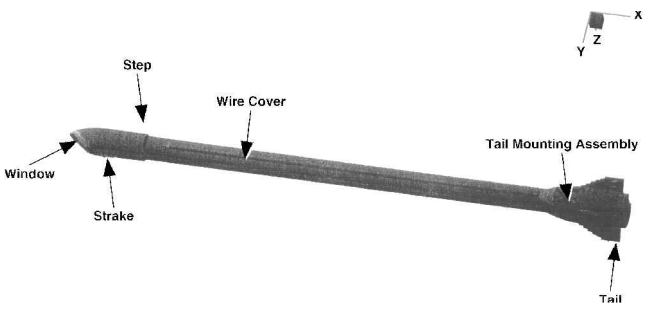

Fig. 1 Geometrical details of a missile with RTV nose.

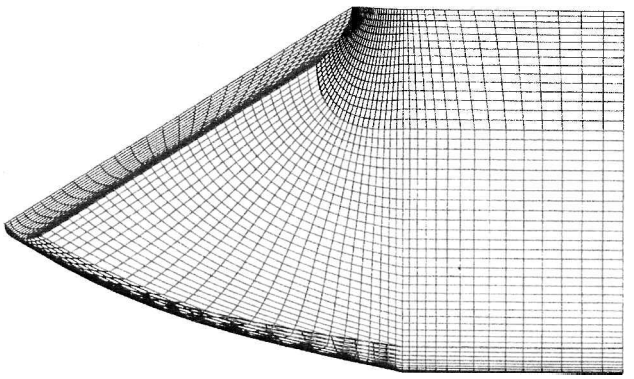

Fig. 2 Grid distribution on missile surface near nose.

for our current studies. PARCH code uses formulations based on the NASA Ames Research Center ARC aerodynamic code and the Arnold Engineering Development Center propulsive extension PARC. This code is particularly suited for missile surfaces because of its grid-patching capability, which is useful for treating embedded surfaces in a flowfield. Patching, that is accomplished in mapped computational coordinates, is automatically constructed from boundary inputs. Boundary conditions are applied along the outer computational boundaries and relevant embedded surfaces. The code uses diagonalized Beam–Warming numerics with matrix-split finite rate chemistry. Several versions of the K-E (kinetic energy and dissipation) turbulence model are available in the code that were specifically developed for jet interaction and propulsive studies. We are currently using the capped low-Reynolds number-formulation[14] for the current simulations.

Typical boundary approaches for the supersonic flows are specified supersonic freestream conditions at the inlet and outer boundaries. Extrapolation procedures are employed at the exit boundary. Surface conditions are appropriate to viscous flows with adiabatic wall condition or specified surface temperature. For subsonic flows exit pressure is specified, whereas inlet and outer boundaries are consistent with local characteristic approach.

The overall grid consists of $192 \times 81 \times 71$ axial, radial, and circumferential points, respectively, for the full missile body. Grid topology was maintained for subsonic, transonic, and supersonic flows, whereas grid points were readjusted with the location of the computational domain boundary. Figure 2 shows an example of the surface grid near the nose of the missile without the nose strake. Local time-stepping procedures with conventional dissipation factors were employed to achieve convergence defined by at least three orders-of-magnitude reduction in the maximum residual. Converged solutions were checked with three and four orders-of-magnitude reduction in the maximum residual for selected cases. The minimum grid spacing near the missile surface was assigned by choosing a y^+ value of 5 for all computations. Variation of this value did not produce any significant changes in the predicted results.

Comparison with Wind-Tunnel Tests

Comparison with the wind-tunnel tests is divided into several parts. First we have studied the body section of the missile without the nose strake, wire cover, fin assembly, and fin i.e., body alone. This comparison was done to understand the modeling aspects of the flat window part of the nose along with the change in diameter by comparing the computed results to the wind-tunnel data. Wind-tunnel tests were also conducted with body alone. Wind-tunnel tests at angles of attack beyond 30 deg showed significant model vibrations. The measured data represent an average of several data readings at a given missile orientation orientation, which were repeatable to within $\pm 10\%$ of the force coefficients. The computational results and their comparisons with the experiments for the subsonic, transonic, and supersonic flows are discussed next.

Subsonic Cases

The subsonic computed cases were compared at a Mach number of 0.8. Table 1 shows comparisons of the computed and experimental values at angles of attack of 20, 30, 40, 50, 60, and 65 deg. These results are also shown in Figs. 3–5. Figure 3 shows a comparison of the normal force coefficients at several angles of attack. At higher angles of attack the computed values are somewhat over

Table 1 CFD and wind-tunnel data comparisons at Mach number = 0.8

	CFD			Wind tunnel		
α, deg	*CN*	*CM*	X_{CP}/D	*CN*	*CM*	X_{CP}/D
20	4.5	8.68	10.42	4.27	10.35	9.9
30	8.69	17.06	10.36	9.37	13.99	10.83
40	14.11	42.9	9.28	15.97	33.42	10.22
50	23.13	38.08	10.67	25.14	41.44	10.67
60	34.49	40.55	11.14	31.74	43.98	10.93
65	41.45	43.5	11.27	33.9	48.23	10.9

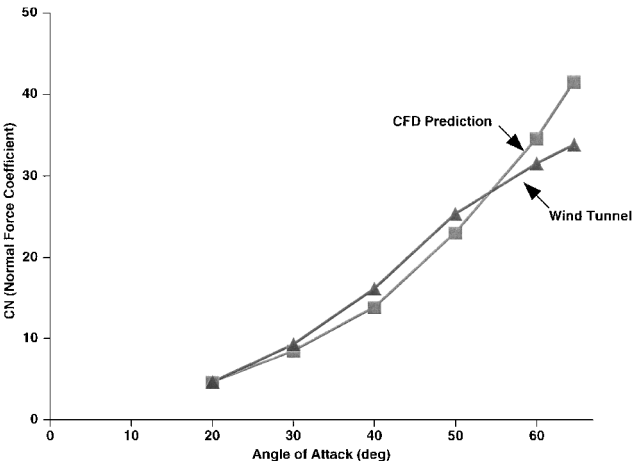

Fig. 3 Comparison of computed and measured normal force coefficient for RTV missile: flow Mach number = 0.8.

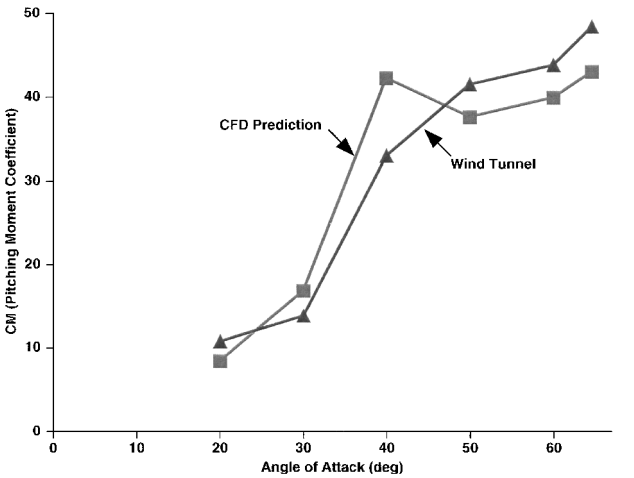

Fig. 4 Comparison of computed and measured pitching moment coefficient for RTV missile: flow Mach number = 0.8.

Table 2 CFD and wind-tunnel data comparisons at Mach number = 0.97[a]

	CFD			Wind tunnel		
α, deg	*CN*	*CM*	X_{CP}/D	*CN*	*CM*	X_{CP}/D
10	2.04	4.93	9.9	1.71	4.87	9.47
30	11.69	20.54	10.56	10.42	33.32	9.1
50	29.1	38.72	10.98	28.46	62.77	12.55
65	41.9	40.19	11.38	38.83	67.72	10.58

[a]Transonic case at $M = 0.97$ gives largest deviation from data for *CM* and X_{cp}/D.

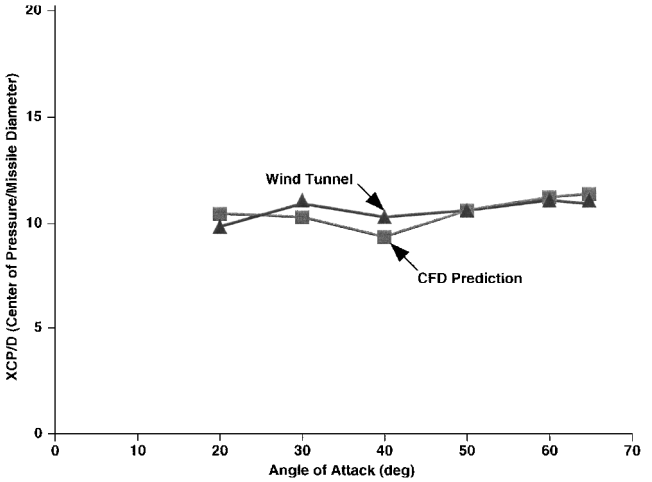

Fig. 5 Comparison of computed and measured center-of-pressure location for RTV missile: flow Mach number = 0.8.

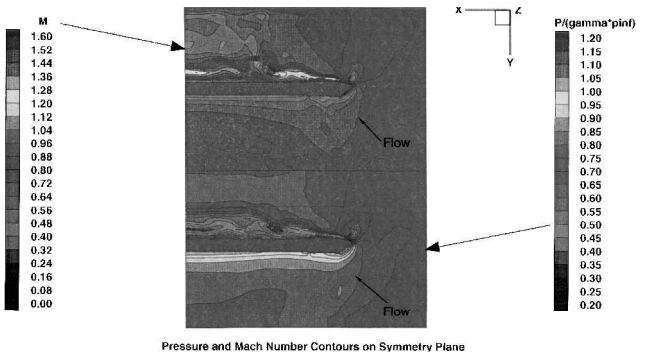

Fig. 6 CFD simulation of RTV missile geometry for subsonic flow: flow Mach number = 0.80, and angle of attack = 50 deg.

predicted. Figure 4 shows a similar comparison for the pitching moment coefficient. The predicted pitching moment coefficients have larger deviations from the wind-tunnel data as compared to the normal force coefficients. A comparison of the center of pressures for these cases is shown in Fig. 5. Despite pitching moment differences, the center-of-pressure locations are predicted well within a missile diameter. Figure 6 shows a plot of the pressure and Mach-number contours on the symmetry plane at this subsonic Mach number of 0.8 and an angle of attack of 50 deg. Large pressures on the windward side and relatively small pressure on the leeward side are observed, which is consistent with the expected flow behavior.

Transonic Cases

Transonic cases were computed at flow Mach numbers of 0.97, 1.05, and 1.2 at angles of attack ranging from 10 to 65 deg. The computational results and the wind-tunnel data comparisons are shown in Tables 2–4. Notice from the preceding tables that the overall comparisons of the predicted force, moment coefficients as well as the center-of-pressure locations with the wind-tunnel data are reasonably good. Figure 7 shows a plot of the pressure and Mach-number contours on the symmetry plane at this transonic Mach number of 1.05 and an angle of attack of 50 deg. Mach-number

Table 3 CFD and wind-tunnel data comparisons at Mach number = 1.05

	CFD			Wind tunnel		
α, deg	*CN*	*CM*	X_{CP}/D	*CN*	*CM*	X_{CP}/D
20	4.62	15.52	8.96	5.05	13.46	9.65
30	10.58	26.82	9.79	10.78	34.31	9.14
40	15.81	48.57	9.25	20.22	49.56	9.87
50	25.18	58.20	10.01	30.91	68.21	10.11
65	35.84	62.25	10.58	42.56	71.46	10.64

Table 4 CFD and wind-tunnel data comparisons at Mach number = 1.2

	CFD			Wind tunnel		
α, deg	*CN*	*CM*	X_{CP}/D	*CN*	*CM*	X_{CP}/D
15	2.67	10.41	8.42	3.2	9.08	9.48
30	10.37	32.51	9.88	11.42	34.8	9.27
40	18.54	44.77	9.91	21.82	40.84	10.45
50	27.84	50.02	10.52	32.98	47.27	10.89
65	42.08	44.54	11.26	43.07	56.90	10.99

Table 5 CFD and wind-tunnel data comparisons at Mach number = 2.0

	CFD			Wind tunnel		
α, deg	*CN*	*CM*	X_{CP}/D	*CN*	*CM*	X_{CP}/D
15	4.12	12.19	9.4	3.47	14.31	8.2
20	7.21	15.24	10.2	6.04	20.37	8.95
27.5	11.86	20.3	10.6	11.28	24.79	10.12

Table 6 CFD and wind-tunnel data comparisons at Mach number = 3.5

	CFD			Wind tunnel		
α, deg	*CN*	*CM*	X_{CP}/D	*CN*	*CM*	X_{CP}/D
15	3.68	10.68	9.42	4.10	13.92	8.92
20	6.13	12.27	10.32	6.56	15.10	10.02
26	8.81	14.42	10.71	10.09	16.96	10.64

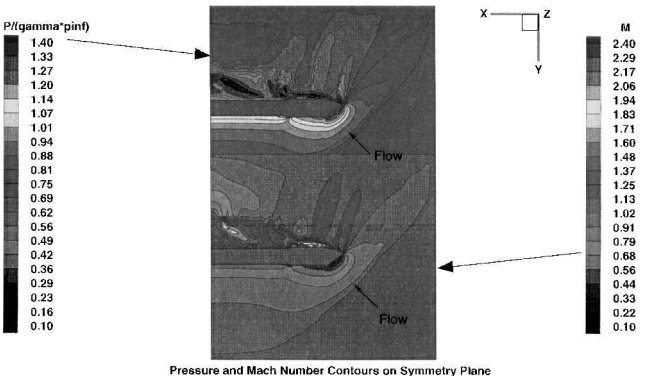

Fig. 7 CFD simulation of RTV missile geometry for transonic flow: flow Mach number = 1.05, and angle of attack = 50 deg.

contours show locally supersonic flow domain on the leeward side caused by rapid expansion around the flat optical window.

Supersonic Cases

Supersonic cases were computed at flow Mach numbers of 2.0, 3.5, and 4.5 at angles of attack ranging from 15 to 26 deg. The angle of attack was limited because of the available data for comparison. Tables 5–7 show the comparisons of the predicted values with the wind-tunnel data. These tables show that the overall comparison of the predicted values of the force, moment, and center-of-pressure locations with the wind-tunnel data is reasonably good. Figures 8 and 9 show the Mach number and pressure contours for freestream Mach numbers of 2.7 and 4.5 at an angle of attack of 26 deg. Notice

Table 7 CFD and wind-tunnel data comparisons at Mach number = 4.5

	CFD			Wind tunnel		
α, deg	*CN*	*CM*	X_{CP}/D	*CN*	*CM*	X_{CP}/D
15	1.7	8.26	7.46	2.09	10.51	7.29
20	3.17	10.36	9.05	3.93	12.00	9.27
26	8.76	12.55	10.86	9.64	15.20	10.74

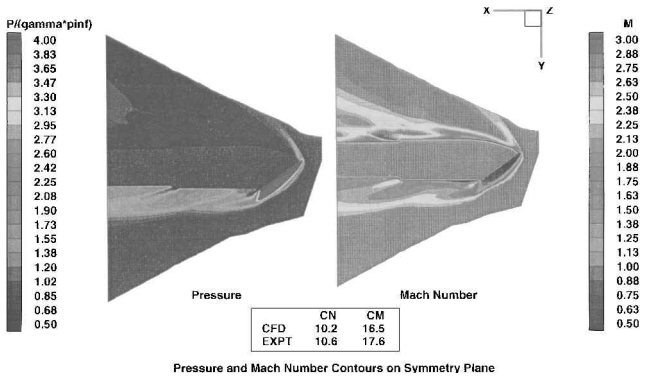

Fig. 8 CFD simulation of RTV missile geometry for supersonic flow: flow Mach number = 2.71, and angle of attack = 26 deg.

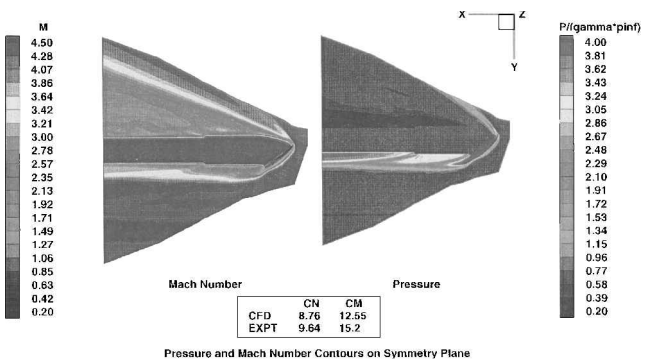

Fig. 9 CFD simulation of RTV missile geometry for high supersonic flow: flow Mach number = 4.5, and angle of attack = 26 deg.

the flow pattern created by the flat optical window as well as the step on the surface of the missile body.

Overall Comparison

Figures 10–12 show the overall comparisons of the predicted results with the wind-tunnel tests for all cases just discussed. Figure 10 shows the normal force coefficients for CFD results and the wind-tunnel tests along with 45-deg perfect match line and lines for $+10/-10\%$ local errors. The cone formed by $+10\%$ error line and -10% error line nearly envelops all of the predicted points indicating the possible error for computed values. Also, the lower magnitudes of the normal force coefficient are better predicted as compared to the experimental data. Figure 11 shows a similar comparison for the pitching moment coefficient. Again the observation is made that the errors in predictions are confined to within $\pm 10\%$ of the experimental values. Figure 12 shows the results for center of pressure location showing similar prediction errors.

Nose-Rolling Moment

A comparison of the nose-rolling moment between computed and measured data was made to establish the validity of the CFD method. This comparison was performed at a Mach number of 2.98 and a zero angle of attack but with a side-slip angle of -15 deg and a missile orientation of -45 deg, without the nose strake (nose strake is used to reduce the nose roll moment). The computed nose roll moment was 2.66 ft-lb, and the measured value was 3.54 ft-lb. This comparison is considered adequate for trend studies during this program. Additional studies may be required to evaluate the origin of these differences. However such studies were precluded by program constraints.

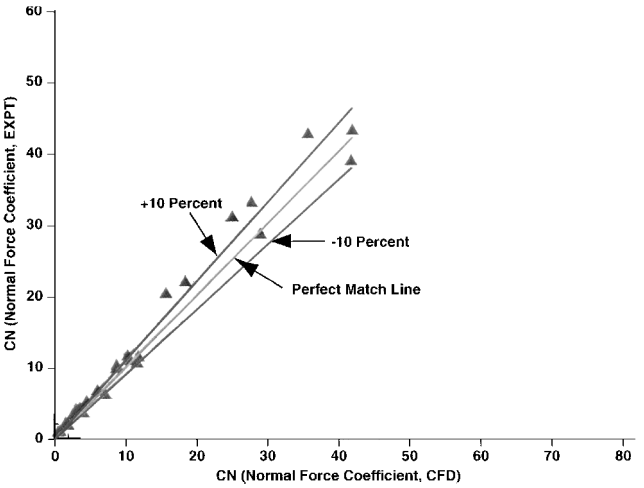

Fig. 10 Normal force coefficient comparison of computation and experiment for RTV missile: Mach number range 0.8–4.5, and angle of attack 10–60 deg.

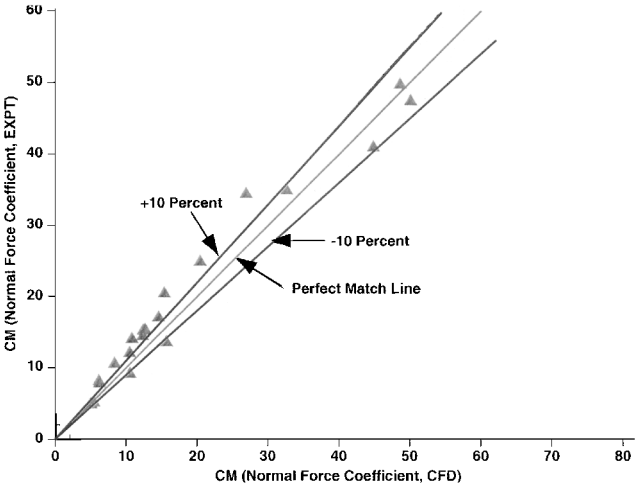

Fig. 11 Pitching moment coefficient comparison of computation and experiment for RTV missile: Mach number range 0.8–4.5, and angle of attack 10–60 deg.

Full Missile Comparison

A large number of design studies were conducted using CFD, based on the basic geometry comparisons as just outlined. Because of cost and time constraints, only a few CFD studies were performed with the full missile geometry. A typical study for the full missile geometry with the optical window in the wind direction and containing nose strake, fin-mounting assembly, and fins in x configuration at a flow Mach number of 2.7 and an angle of attack of 26 deg is discussed next.

Figures 13–15 show the computational results for the full missile geometry. Figure 13 shows the pressure distribution on the missile surfaces at these conditions. From this figure notice the high pressure on the optical window, side faces, fin-mounting assembly, and windward fins. Figure 14 shows a plot of the total pressure distribution in the flowfield at several axial locations. This figure shows the vortex patterns formed on the leeward side of the missile body typified by the low total pressures. Figure 15 shows a comparison of the computed force and moment coefficients with the wind-tunnel data as well as component load distribution for the missile. The overall comparison of the predicted value with the wind-tunnel data is reasonably good.

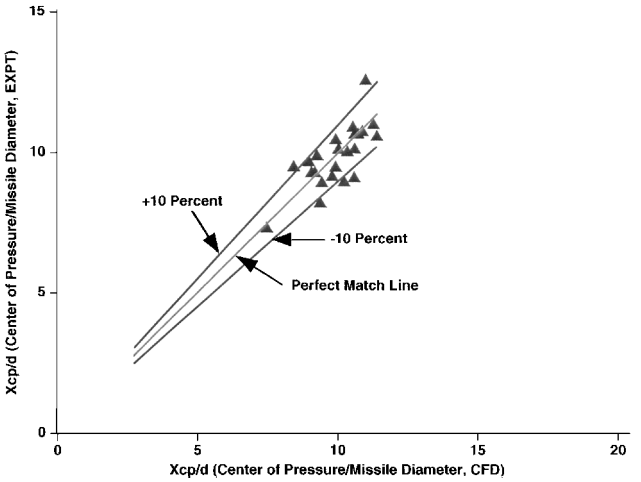

Fig. 12 Center-of-pressure comparison of computation and experiment for RTV missile: Mach number range 0.8–4.5, and angle of attack 10–60 deg.

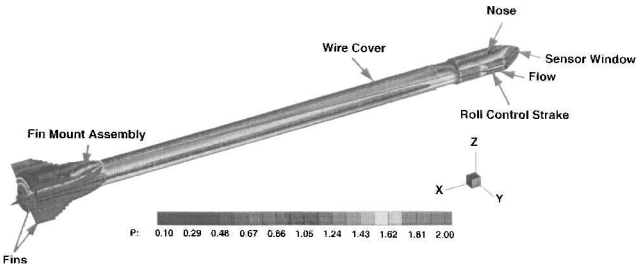

Fig. 13 Surface pressure distribution for RTV missile geometry: flow Mach number = 2.7, angle of attack = 26 deg, and window windward.

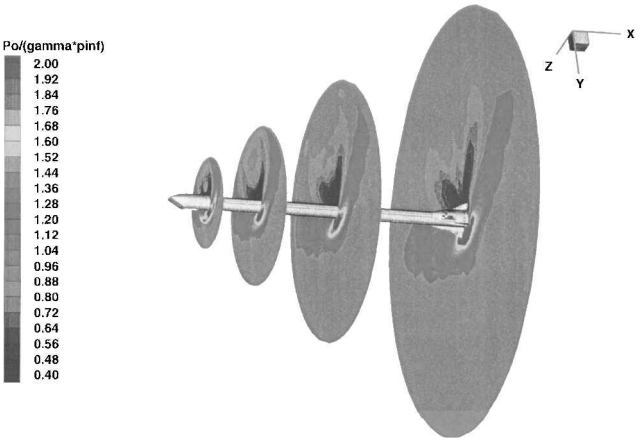

Fig. 14 Total pressure distribution for several missile axial locations: flow Mach number = 2.7, angle of attack = 26 deg, and window windward.

Results and Discussion

Multibody Interference Effects

Two CFD application studies are presented to demonstrate the utility of such design tools for providing cost-effective rapid estimates of design data during the preliminary missile design phase. One relates to captive flight interference effects specifically for the RTV missile. Concerns relating to the required nose-rolling moment in captive flight (with multibody interactions) for onboard motor design (required torque for wide-angle sensor viewing) necessitated this preliminary study. A suitable model for this study is shown in Fig. 16. The model consists of two RTV missiles mounted on pylons in the vicinity of starboard wing of the carrier aircraft. All of the dimensions were obtained from a current carrier aircraft. A computational grid for this model consisted of 137 × 103 × 145 axial,

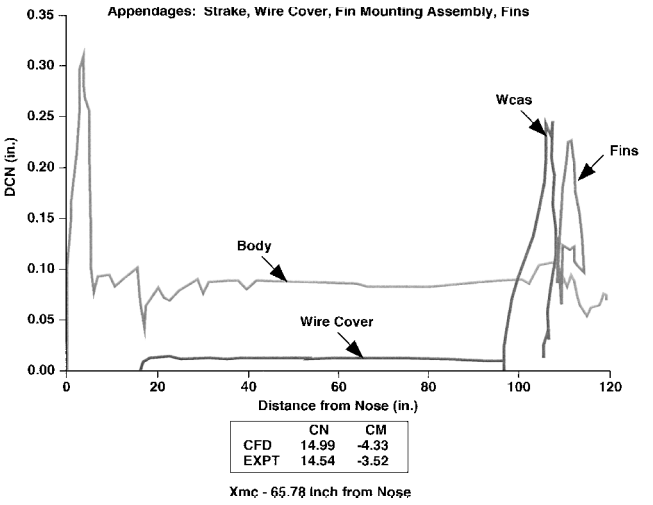

Fig. 15 Load distribution on the missile components and comparison with wind-tunnel measurements: flow Mach number = 2.71, angle of attack = 26 deg, and windward window.

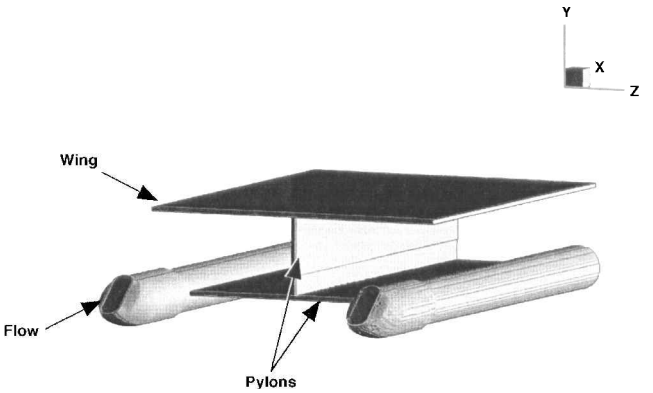

Fig. 16 Geometry for CFD simulation of RTV missiles with wing and pylons.

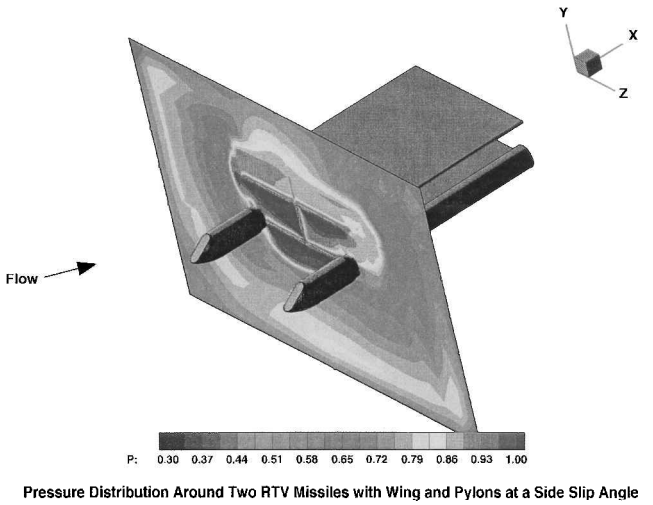

Fig. 17 CFD simulation of RTV missiles with wing and pylons: flow Mach number = 1.2, angle of attack = 10 deg, and side slip = 45 deg.

radial, and circumferential points, respectively. Figure 17 shows a computed result for this simulation with a carrier aircraft flight Mach number of 1.2, an angle of attack of 10 deg, and a side-slip angle of attack of 45 deg. The results in this figure show pressure distribution on a vertical plane downstream of the RTV nose. This figure shows that the interaction process creates an asymmetric flow pattern with different rolling moments on the two RTV missiles. The total computed sea-level nose-rolling moments are 0.75 ft-lb (1.19 ft-lb on

the nose and −0.45 ft-lb because of the strake) on the left RTV missile and 1.16 ft-lb (1.45 ft-lb on nose and −0.29 ft-lb because of strake) on the right RTV missile. Compare this with the computed free-flight nose-roll moment of 1.106 ft-lb (1.277 ft-lb on nose and −0.1706 ft-lb because of strake) at the same conditions. Interference effects at these conditions reduced the overall nose-roll moment as compared to the free-flight value. Several other cases were computed to show the interference effects at various flight conditions during the design process.

Optical Distortion

The second application study relates to aero-optical analysis of the RTV window using a coupled CFD-optical methodology. The current study deals with the optical beam distortion caused by the ordered flow disturbances around the flight vehicles such as shock-induced density disturbances around the vehicle, compressible boundary-layer effects, i.e., density gradient near the window wall and heat-transfer effects to the window wall.

The density effects just described can be extremely complex because of the presence of the nose shock around the geometry, its interaction with the near-wall flow, embedded shocks and expansions near the window-body interface, window recess, and the window wall condition. It may be possible to assess these effects grossly using approximate methods, but their applicability to such a complex environment will be highly suspect. However, the advent of new analysis methodologies such as CFD offer a promising alternative for assessing these effects. The current study uses a fully validated CFD approach to predict the optical distortion during critical flight conditions. The details of this approach and the results are described next.

Figure 1 shows the external geometry of the RTV missile for flow modeling. The nose part of this geometry was used to perform CFD simulation using a FNS solver with a K-E turbulence model to predict the flow properties around the missile body for a specific flight condition. The predicted flow properties were compared with the wind-tunnel tests to validate the predictions by comparing the predicted force and moment coefficients with the measured data as discussed before. The detailed flow structure was then synthesized for optical computations.

The seeker positions defining the sensor looks are depicted in Fig. 18. For a given seeker position the optical computation method primarily uses the CFD-computed three-dimensional flowfield (density field) to create slices of $z =$ constant planes (see Fig. 1 for the axis system) for a user specified two-dimensional grid through advanced interpolation techniques. This density database is then used to do the following:

1) Determine the optical path length for a given sensor orientation: for example, see Fig. 19, which shows the density variation along several rays of light for two orientations of the seeker. Note from this figure that the density field decreases to the freestream value over a certain length, which is dependent on the path of the ray. The optical path length for this sample case is then about 2.5 in., which is the maximum distance of active density perturbations from the window along a ray.

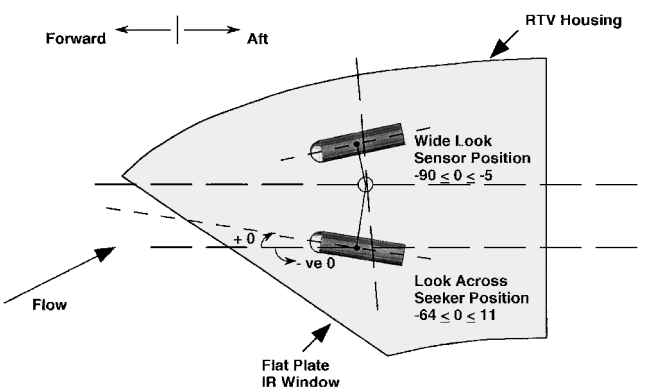

Fig. 18 Seeker positions defining sensor looks.

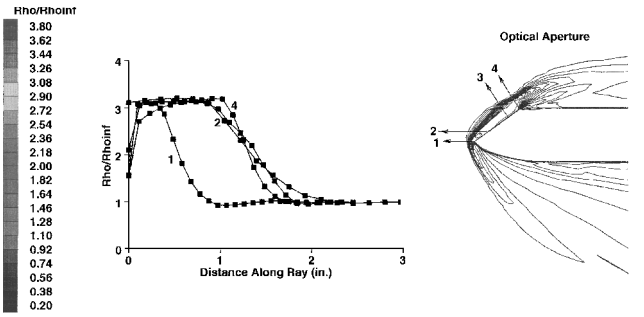

Fig. 19 Optical fidelity studies for RTV flat-plate window: flow Mach number = 2.7, angle of attack = 26 deg, and optical plane at $Z = 1.0$ in.

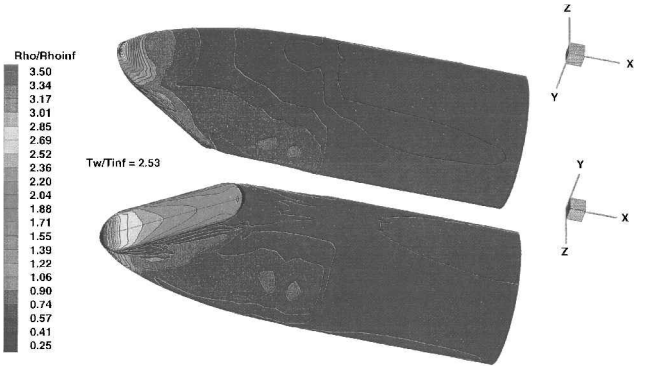

Fig. 20 Surface density distribution for RTV missile nose: flow Mach number = 3.0, and angle of attack = 5 deg.

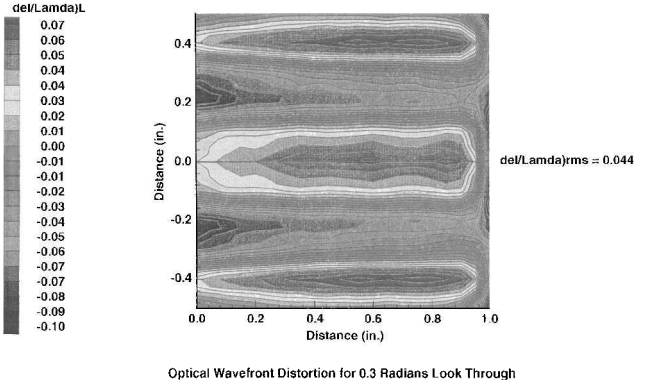

Fig. 21 Optical fidelity studies for RTV missile window: flow Mach number = 3.0, angle of attack = 5 deg, and plane fit = 1.3539*x-0.097076*y-0.65394.

2) Determine the density variation across the rays for a square in beam aperture using all z-planes density data. All density perturbations are computed as $(\rho_{local} - \rho_{avg})/\rho_{avg}$ (where ρ_{avg} is the average density for the entire optical volume and ρ_{local} is the local density averaged along the optical path) for the entire optical volume (yields two-dimensional density perturbations data).

3) Determine the optical path length distortion based on the preceding density data using the Gladstone–Dale constant, which relates the density perturbations to the index of refraction perturbations.

4) Determine the wedge angle for the optical aperture using a least-square surface fit to the two-dimensional optical path length distortion from the preceding. This wedge angle is removed from the two-dimensional optical path length distortion data to yield wedge-corrected wavefront distortion for the beam aperture. Root-mean-square values are used to convert this two-dimensional data to a point data for a given sensor orientation.

Figure 20 shows the density plot for a case computed at a flight Mach number of 3.0 and an angle of attack of 5 deg. Figure 21 shows a corresponding plot for optical wave front distortion for 0.3 radian

look angle at these flight conditions. Note from this figure that an overall root mean square value of 0.044 waves after correction is obtained. The data obtained from several such computations were used for optical design definition.

Conclusions

Computations were performed for a RTV missile with a flat optical nose window at freestream Mach numbers of 0.8, 0.97, 1.05, 1.2, 2.0, 3.5, and 4.5 and at angles of attack ranging from 10 to 65 deg. The computed results show good comparisons with the experimental data (error bound to $\pm 10\%$ from the experiment) for body alone (with optical window at the nose), good comparisons for the full missile (includes body, nose strake, wire cover, fin assembly, and fins) and nose roll moment. Design studies are then performed to estimate the steady-state multibody effects for a captive-flight scenario and optical quality of the sensor window.

References

[1]Srivastava, B. N., "Lateral Jet Effectiveness Studies for a Missile Using Navier–Stokes Solutions," AIAA Paper 11-08 alt, Sept. 1996.

[2]Srivastava, B. N., "Lateral Jet Control of Supersonic Missile: CFD Predictions and Comparisons to Force and Moment Measurements," *Journal of Spacecraft and Rockets*, Vol. 35, No. 2, 1998, pp. 140–146: also AIAA Paper 97-0639, Jan. 1997.

[3]Srivastava, B. N., "CFD Analysis and Validation for Lateral Jet Control of a Missile," *Journal of Spacecrafts and Rockets*, Vol. 34, No. 5, 1997, pp. 584–592; also AIAA Paper 96-0288, June 1996.

[4]Srivastava, B. N., "Lateral Jet Control of a Supersonic Missile: Computational Studies with Forward, Rear Body and Wing Tip Mounted Jets" *Journal of Spacecraft and Rockets*, Vol. 35, No. 3, 1998, pp. 278–286; also AIAA Paper 97-2247, June 1997.

[5]Srivastava, B. N., "Asymmetric Lateral Jet Interaction Studies for a Supersonic Missile: CFD Prediction and Comparison to Force and Moment Measurements," *Journal of Spacecraft and Rockets*, Vol. 36, No. 5, 1999, pp. 621–632; also AIAA Paper 98-2410, June 1998.

[6]Srivastava, B. N., Furtek, J., Shelton, A., and Paduano, R., "Role of CFD in Missile Aerodynamic Design: Review of Recent Efforts at Raytheon," NATO, *RTO Meeting Proceedings on Missile Aerodynamics*, RTO-MP-5, Paper 33, Sorrento, Italy, May 1998, pp. 33-1–33-19.

[7]Degani, D., and Schiff, L. B., "Computation of Turbulent Supersonic Flows Around Pointed Bodies Having Cross Flow Separation," *Journal of Computational Physics*, Vol. 66, No. 1, 1986, pp. 173–196.

[8]Schiff, L. B., Degani, D., and Gavali, S., "Numerical Simulation of Vortex Unsteadiness on Slender Bodies of Revolution at Large Incidence," AIAA Paper 89-0195, Jan. 1989.

[9]Ekaterinaris, J. A., "Analysis of Flow Fields over Missile Configurations at Subsonic Speeds," *Journal of Spacecraft and Rockets*, Vol. 32, No. 3, 1995, pp. 385–391.

[10]Hsieh, T., Priolo, F. J., and Wardlaw, A. B., Jr., "Navier-Stokes Calculation of Flow over a Complete Missile to 60 deg Incidence," AIAA Paper 95-0760, Jan. 1995.

[11]Smith, E. H., Hebbar, S. K., and Platzer, M. F., "Aerodynamic Characteristics of a Canard-Controlled Missile at High Angles-of-Attack," *Journal of Spacecraft and Rockets*, Vol. 31, No. 5, 1994, pp. 766–772.

[12]Tuncer, I. H., Marvin, R., and Platzer, M. F., "Numerical Investigation of Subsonic Flow over a Typical Missile Fore Body," AIAA Paper 96-0189, Jan. 1996.

[13]York, B. J., Sinha, N., Kenzakowski, D. C., and Dash, S. M., "PARCH Code Simulation of Tactical Missile Plume/Airframe/Launch Interactions," *19th JANNAF Exhaust Plume Technology Meeting*, Chemical Propulsion Information Agency PWB, May 1991, pp. 645–674.

[14]Dash, S. M., Sinha, N., York, B. J., Lee, R. A., and Hosangadi, A., "On the Inclusion of Advanced Turbulence Models and Nonequilibrium Thermochemistry into State-of-the-Art CFD Codes and Their Validation," AIAA Paper 92-2764, May 1992.

R. M. Cummings
Associate Editor